npj | flexible electronics

Article

Published in partnership with Nanjing Tech University

https://doi.org/10.1038/s41528-025-00483-8

Topological optimization of heterogeneous strain structures for computational design of ultra-sensitive strain sensors

Weijuan Wang[1], Ting Yui Wong[2], Minghao Guo[1], Fangxin Zou[1] ✉, Fuhong Chen[3,4] & Zhiwei Wang[3,4,5]

Heterogeneous strain engineering offers a promising approach for developing high-performance stretchable strain sensors, but the optimal strain distributions remain unexplored. Herein, we derive the optimal strain topology for achieving maximum sensitivities using Monte Carlo simulations, and identify the key sensitivity-regulating parameters, thus establishing a general computational design guideline. Mathematical analysis demonstrates that within the optimal topology, sensitivity is maximized by reducing the strain value of low-strain regions or increasing their area proportion. As proof of concept, patterned graphene strain sensors (PGSSs) featuring parameterized grooves are designed with their small strain values and proportions precisely modulated via finite element analysis. Adjusting these parameters enhances sensitivity by factors of ~10.7 and 3.3, with the highest gauge factor reaching 25,600 at 100% strain. Furthermore, the PGSSs can effectively detect human body motions and gauge object dimensions when integrated with robot grippers. The computational framework exhibits applicability across different heterogeneous strain engineering methods.

Flexible and stretchable strain sensors have garnered significant interest due to their indispensable role in contemporary technological applications, including wearable electronics, soft robotics, and biomedical devices[1–3]. Basically, resistive strain sensors featuring convenient signal acquisition, cost-effective fabrication, and simple device configuration have emerged as the most ideal contenders for strain sensing technology[4,5]. With the escalating demand for more intelligent human-machine interfaces and sophisticated monitoring of complex biological signals, the development of highly sensitive stretchable strain sensors has gained prominence[6–8]. These sensors excel in accurately converting mechanical stimuli into digital signals, enabling enhanced interaction and monitoring capabilities in diverse applications. Over the past few years, significant efforts have been invested in the exploration of highly sensitive conductive active materials and structures, such as carbon-based materials[9,10], auxetic mechanical metamaterials[11,12], bionic structures[13,14], and multilayer structures[15,16], with the fundamental design principle centered on constructing effective conductive networks either within the bulk polymer or on its surface. However, achieving a high gauge factor remains a grand challenge, especially under large strain conditions[17].

Recently, heterogeneous strain engineering (Fig. 1a), which involves manipulating strain-induced electrical signals at the microscale, has emerged as a powerful strategy to optimize conductive networks[18–24]. Various microengineering techniques[18–20] and heterogeneous elastomer substrates[24,25] are employed to facilitate the construction of heterogeneous strain distributions in strain sensors. The theoretical foundation of this strategy is based on the decomposition of an applied strain into multiple strain levels within the sensing material and is underpinned by the recognition that the resistance response of a single sensing material varies across different strain levels, with resistance typically increasing as strain intensifies (Fig. 1b). Locally amplified strains induce significant spatial separation of conductive elements, which substantially increases local resistance[17], thereby regulating the electron transport path. Notwithstanding significant advancements, previous literature offers limited discussion regarding the optimal heterogeneous strain distributions that would output maximum

[1]Department of Aeronautical and Aviation Engineering, The Hong Kong Polytechnic University, Hung Hom, Kowloon, Hong Kong SAR, China. [2]Department of Civil and Environmental Engineering, The Hong Kong Polytechnic University, Hung Hom, Kowloon, Hong Kong SAR, China. [3]Centre for Quantum Physics, Key Laboratory of Advanced Optoelectronic, Quantum Architecture and Measurement (MOE), School of Physics, Beijing Institute of Technology, Beijing, 100081, China. [4]Beijing Key Lab of Nanophotonics and Ultrafine Optoelectronic Systems, Beijing Institute of Technology, Beijing, 100081, China. [5]Beijing Institute of Technology, Zhuhai, 519000, China. ✉e-mail: frank.zou@polyu.edu.hk

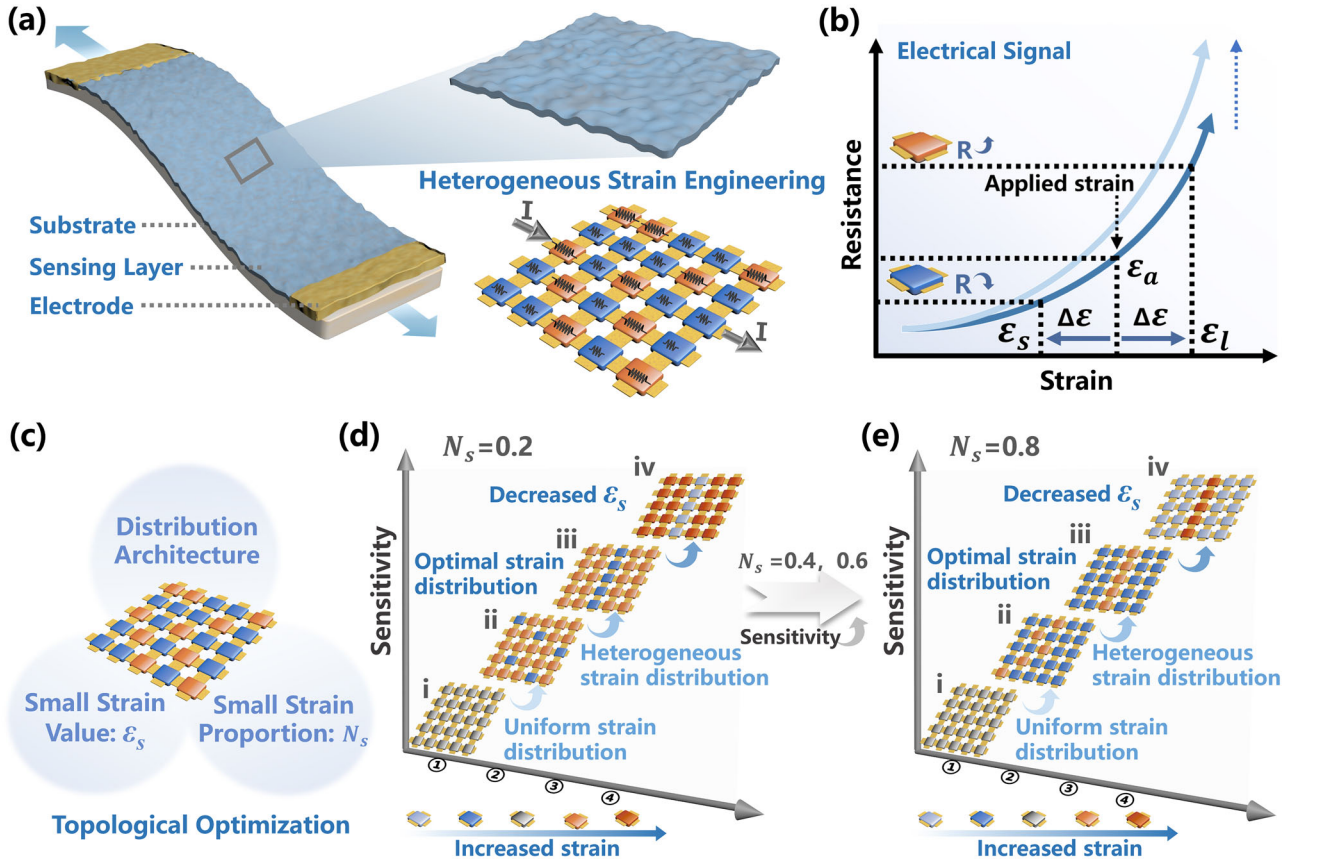

Fig. 1 | Conceptualization of topological optimization of the heterogeneous strain framework. a Architecture of a heterogeneous strain-engineered sensor. **b** Sensitivity enhancement principle of heterogeneous strain engineering based on the decomposition of an applied strain into small strain (ε_s) and large strain (ε_l) components. **c** Multi-parameter optimization framework incorporating distribution architecture, ε_s, and small strain proportion in each row (N_s). **d** Topological optimization at fixed N_s: (i) uniform strain distribution, (ii) heterogeneous strain distribution, (iii) optimal heterogeneous strain topology, (iv) decreased ε_s for sensitivity enhancement. **e** Increased N_s for further sensitivity optimization under fixed ε_s.

sensitivities, attributable to the unclear fundamental structure-property relationship between microscale local strain and macroscopic sensing performance. Additionally, this knowledge gap complicates the formulation of quantitative design guidelines applicable to various sensor fabrication methods.

To address this challenge, a theoretical framework for the topological optimization of heterogeneous strain-based sensors is established for the first time in this work, integrating the macroscopic sensing performance of strain sensors with their local strains at the microscale. The Monte Carlo method is employed as a computational tool to simulate this framework, enabling derivation of the optimal heterogeneous strain topology and identification of the key parameters governing sensing performance, which in turn guide the computational design of ultra-sensitive strain sensors (Fig. 1c–e). The Monte Carlo simulation results reveal that random heterogeneous strain distributions with different combinations of small strain coefficient and small strain proportion can lead to either increased or decreased sensitivity relative to the non-heterogeneous strain distribution condition, depending on their exact topological configurations. Upon focused analysis of the heterogeneous strain topology that yields the maximum sensitivities, a general design guideline for heterogeneous strain-based sensors is formulated, where sensing performance can be enhanced by either reducing the strain value of low-strain regions or increasing the proportion of low-strain regions, both of which amplify the strain value of localized high-strain regions. The underlying mechanisms are substantiated through mathematical proofs, providing a theoretical foundation for computational design of ultra-sensitive strain sensors.

As proof of concept, we designed patterned graphene strain sensors (PGSSs) featuring the optimal heterogeneous strain topology by engineering parameterized grooves on flexible substrates. These designs differ systematically in either the strain value of low-strain regions or the proportion of low-strain regions. Multiphysics finite element analysis (FEA) models of the PGSSs were formulated to quantitatively predict sensing responses, thereby facilitating programmable structural design and virtual verification. By precisely controlling the variations in the two key parameters, the sensing performance of PGSSs achieves high tunability and predictability, exhibiting an enhancement in sensitivity by factors of approximately 10.7 and 3.3. The maximum gauge factors of the two sets of PGSSs were 25,600 and 17,800, respectively, far surpassing that of unpatterned graphene strain sensors (i.e., 840). The PGSSs demonstrate reliable detection of human body motions as well as accurate feedback of object dimensions when integrated with a robot gripper. This optimal heterogeneous strain topology has also been successfully extended to other sensor systems, demonstrating the universality of the quantitative design guideline across various sensor fabrication methods.

Results

Topological optimization of heterogeneous strain structures

A Monte Carlo method-based model was established to simulate the stochastic distribution of heterogeneous strains and investigate the effects of heterogeneous strain parameters on the macroscopic resistance behaviors of strain sensors. As illustrated in Fig. 2a, the simulation approach is based on the representation of a sensing area by a 2D (5×5) matrix of unit cells, where each unit cell exhibits a uniform strain and the corresponding resistance. Figure S1 shows the equivalent resistor network. Under a uniform strain distribution, the strain within each cell is equal to the externally applied strain. When heterogeneous strains are incorporated, it is assumed that within the sensing area, there are two types of strains that are

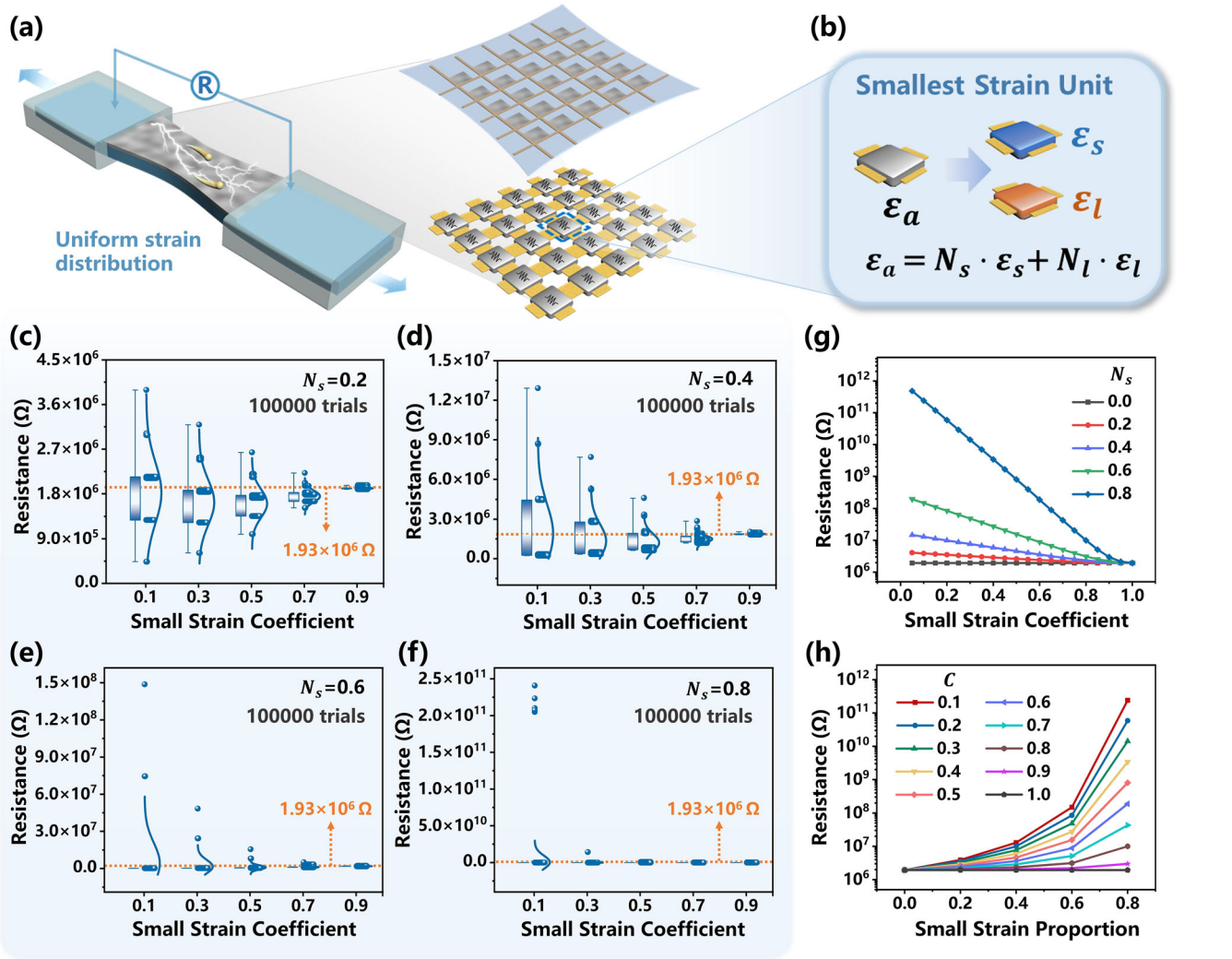

Fig. 2 | Topological optimization of the heterogeneous strain framework guided by the Monte Carlo method. a Schematic of a strain sensor under uniaxial tension, with the sensing area depicted as a 5 × 5 grid of strain units. **b** Introduction of heterogeneous strains. **c**–**f** The resistances under randomly generated heterogeneous strain distributions (100,000 trials per fixed N_s and C parameter set) at 100% applied strain, with the dashed lines representing the resistance under uniform strain distribution. **g**, **h** The relationships between maximum resistance, small strain proportion and small strain coefficient, at 100% applied strain.

respectively lower and higher than the applied strain, denoted as small strain (ε_s) and large strain (ε_l) (Fig. 2b). These small and large strains are randomly distributed across the 2D matrix of unit cells. It is worth noting that along the direction of the applied strain, the mean strain of each row in the matrix equals the applied strain (ε_a), as illustrated by the following formula:

$$N_s\varepsilon_s + N_l\varepsilon_l = \varepsilon_a \tag{1}$$

where N_s and N_l stand for the small strain proportion and large strain proportion in each row, respectively, with $N_s + N_l = 1$. Within this model, small strain value, which can only vary from 0 to ε_a, is selected as the parameter for regulating heterogeneous strains, thereby allowing for easier control of parameter ranges. A small strain coefficient C $(0 < C < 1)$ is therefore introduced, such that $\varepsilon_s = C\varepsilon_a$, and Eq. (1) is reformulated as:

$$N_sC\varepsilon_a + (1 - N_s)\varepsilon_l = \varepsilon_a \tag{2}$$

Firstly, an exponential resistance-strain relationship was obtained experimentally under a uniform strain distribution (Fig. S2), serving as the foundation for subsequent Monte Carlo simulations of heterogeneous strain distributions. Then, the total resistance of the sensing system was computed through Monte Carlo simulations, where each unique combination of small strain proportion and small strain coefficient was evaluated across 100,000 randomly generated heterogeneous strain distributions, all under a consistent 100% applied strain (Fig. 2c–f). The results of the randomized simulations demonstrate that compared to the uniform strain distribution condition, a heterogeneous strain distribution can either increase or decrease the resistance of the system. This variability depends on the topological structure of the heterogeneous strain, i.e., the relative positions of the small strain units and large strain units, as well as on the small strain proportion and small strain coefficient. If small strain units (low-resistance domains) are able to form a percolating network, electric current will preferentially flow through these parallel low-resistance paths, resulting in reduced overall resistance. Conversely, if all continuous low-resistance pathways are disrupted by large strain units (high-resistance domains), current will be forced through series-connected bottlenecks, leading to significantly enhanced resistance. In the following analysis, we focus solely on the heterogeneous strain distributions that lead to the maximum resistance under any combination of small strain proportion and small strain coefficient. As shown in Fig. 2g, resistance increases when small strain proportion remains constant while small strain coefficient decreases. Conversely, maintaining small strain coefficient constant, an increase in small strain proportion results in an increase in resistance (Fig. 2h). The

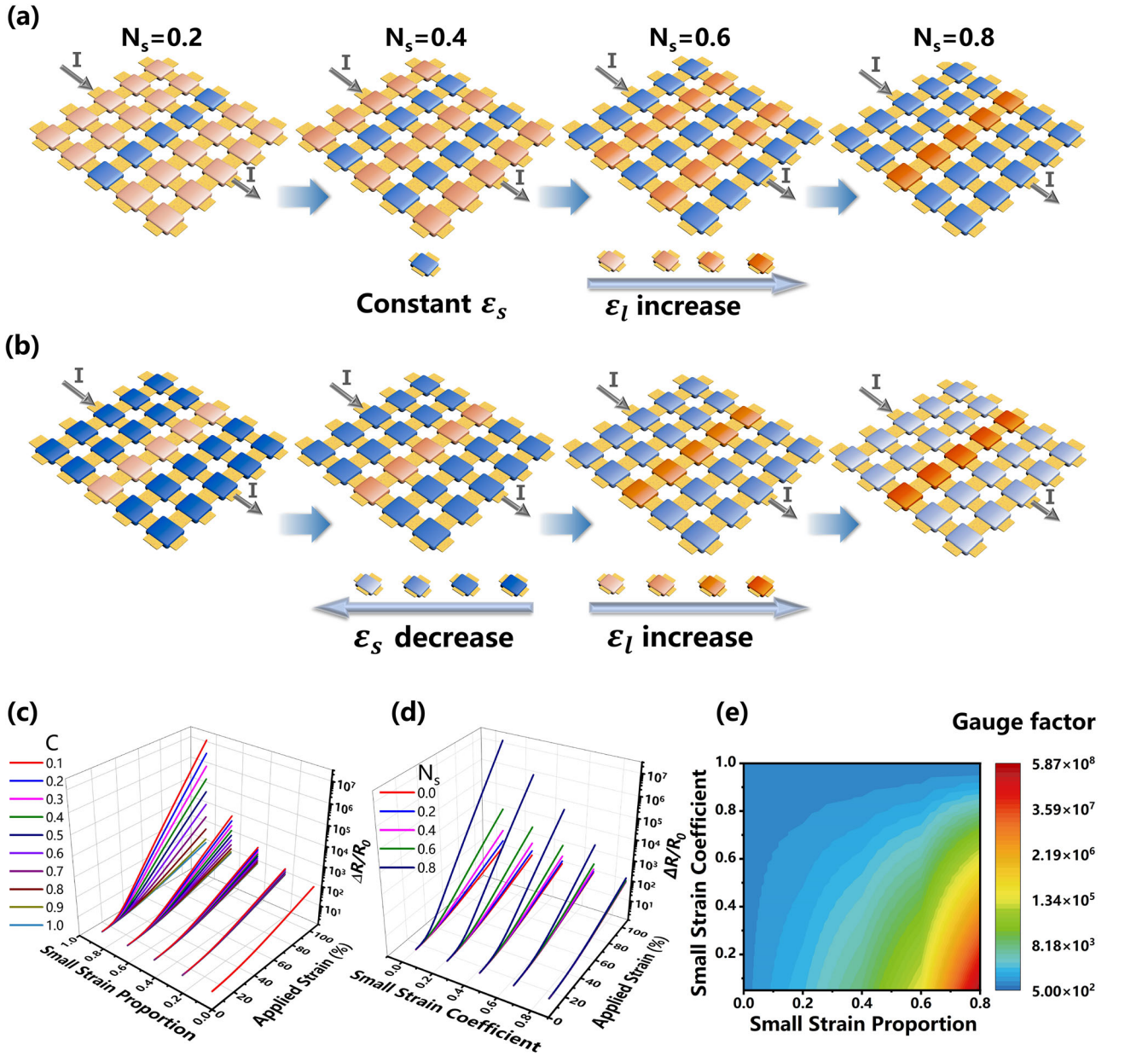

Fig. 3 | The optimal heterogeneous strain topology and the corresponding sensing performance. a The heterogeneous strain distributions that lead to the maximum resistance under progressively increasing small strain proportions and a constant small strain coefficient. **b** The heterogeneous strain distributions that lead to the maximum resistance under gradually decreasing small strain coefficients and a constant small strain proportion. **c**, **d** The relative resistance change-strain responses under various small strain coefficients and small strain proportions. **e** The contour map of sensitivity at 100% applied strain.

decrease in small strain coefficient and the increase in small strain proportion are both aimed at amplifying large strain value (Fig. S3). In addition, the phenomenon that the incorporation of diverse strain levels within a sensing system leads to higher resistance can be easily observed, as $N_s = 0$ or $C = 1$ signifies the state of uniform strain distribution.

The configurations of the heterogeneous strain distributions that yield the maximum resistance under different small strain proportions are derived, as demonstrated in Fig. 3a. All large strain units are arranged in a column and aligned perpendicularly to the direction of the electric current. The total resistance under such strain distribution can be calculated as follows:

$$R_{total} = N_s R(\varepsilon_s) + N_l R(\varepsilon_l) \tag{3}$$

where $R(\varepsilon_s)$ and $R(\varepsilon_l)$ are the local resistance of the small strain units and the large strain units, respectively. Thus, it can be mathematically proven that, firstly, the total resistance under an optimal heterogeneous strain distribution consistently surpasses that under a uniform strain distribution, as illustrated by the following inequality (see Supplementary Note S1.1 for details):

$$N_s R(\varepsilon_s) + N_l R(\varepsilon_l) > R(\varepsilon_a) \tag{4}$$

and secondly, when small strain coefficient is fixed, an increase in small strain proportion amplifies large strain value (Fig. 3a), in turn exponentially increasing the local resistance of large strain units and consequently leading to an increase in total resistance (see Supplementary Note S1.2 for details). Figure 3b depicts the heterogeneous strain distributions in which large strain value increases as small strain coefficient decreases, with the example provided being N_s set to 0.8. As also proven mathematically, the accumulation of local strain, which results in the amplification of large strain value, leads to an increase in total resistance (see Supplementary Note S1.3 for details). The

impact of small strain coefficient and small strain proportion on strain sensing response is illustrated in Fig. 3c, d. The sensitivity of a strain sensor is evaluated by monitoring the relative resistance change ($\Delta R/R_0$), where R_0 denotes the initial resistance, and ΔR represents the variation in resistance when subjected to strain[26,27]. Under any applied strain, when small strain proportion is held constant, a decrease in small strain coefficient results in an increase in $\Delta R/R_0$, signifying enhanced sensitivity. Conversely, maintaining a constant small strain coefficient while increasing small strain proportion also leads to higher $\Delta R/R_0$. Figure 3e depicts the gauge factors at 100% applied strain, from which we can clearly observe the trend of sensitivity variation correlating with changes in small strain coefficient and small strain proportion. Therefore, a quantitative design guideline for strain sensors featuring the optimal heterogeneous strain topology is drawn, whereby sensing performance can be enhanced by decreasing small strain values or increasing small strain proportions.

To ascertain the criticality of exponential resistance-strain relationships to heterogeneous strain engineering, we artificially established a linear resistance-strain relationship and conducted analogous Monte Carlo simulations to investigate the characteristics of resistance variations within a heterogeneous strain distribution landscape. The linear resistance-strain relationship was established by setting the initial resistance and the resistance at 100% applied strain to align with experimentally obtained data (Fig. S4). The results of the randomized simulations indicate that the maximum resistance within the heterogeneous strain distribution landscape can only equate to the resistance under uniform strain distribution (Fig. S5), thus negating any enhancement of sensitivity. The Monte Carlo simulation results for both types of relationships suggest that the above heterogeneous strain engineering, designed to augment sensitivity, is only applicable to systems with an exponential resistance-strain relationship. For linear systems, the adoption of heterogeneous strain distributions does not enhance sensitivity and may even lead to a decrease in sensitivity.

Computational structural design of PGSSs

With the programmable computational approach, we designed a PGSS exhibiting the theoretically optimal heterogeneous strain topology derived from Monte Carlo simulations and established a corresponding FEA formulation (Fig. 4a). The upper layer of the strain sensor consists of a graphene sensing layer, while the lower layer is composed of a PDMS substrate that incorporates grooves perpendicular to the tensile direction. The grooved regions can be considered areas of stress concentration, i.e., large strain areas, while the regions between the grooves can be regarded as small strain areas. Such configuration embodies continuous columns of large strain units that completely disrupt potential low-resistance pathways, forcing all charge carriers to traverse series-connected high-resistance bottlenecks. When the patterned flexible substrate is subjected to external stretching, it causes the graphene on its surface to move, effectively transferring the strain state to the sensing layer (Fig. S6). The strain sensing response of the PGSS can be quantitatively evaluated using the constructed FEA formulation, which incorporates electro-mechanical coupling. By utilizing the resistance change-strain relationship of an unpatterned graphene strain sensor (Fig. 4b(i)), coupled with the surface strain distributions of the PGSS (Fig. 4b(ii)), we can calculate the electric potential distributions in the PGSS, thereby obtaining the corresponding resistance responses (see Methods Section for details). Such computational design approach, based on Multiphysics coupling, opens new avenues for programmable structural design and quantitative sensitivity prediction for strain sensors.

The Monte Carlo simulation results indicate that for sensors featuring the optimal heterogeneous strain topology, sensitivity is inversely proportional to small strain value when small strain proportion remains unchanged. Conversely, with a fixed small strain value, sensitivity increases as small strain proportion rises. To corroborate the effectiveness of the two key control parameters, six PGSSs with different structural configurations were systematically designed, with their structural parameters depicted in Fig. S7. The small strain values and small strain proportions can be modulated through strategic variations of groove depth and inter-groove spacing on the flexible substrates. The first set of PGSSs displays a consistent inter-groove spacing of 400 μm, while featuring groove depths of 40, 60, and 80 μm. In the second set of PGSSs, the inter-groove spacings are set to be 200, 250, and 300 μm, with corresponding groove depths of 60, 70, and 80 μm. The six structural patterns are categorized and labeled according to their respective groove depths and inter-groove spacings, denoted as 40–400, 60–400, 80–400, 60–200, 70–250, and 80–300. Figure 4c, d present the FEA results of the heterogeneous strain distributions of the six distinct structural patterns when subjected to 100% applied strain. It can be observed that the strain levels within the grooved regions are substantially elevated compared to the applied strain, while the strain levels in the inter-grooved regions are significantly reduced. In Fig. 4c, the small strain area sizes remain consistent, signifying a constant small strain proportion. However, the small strain values incrementally decrease, which can be attributed to the increase in groove depth from 40 μm to 80 μm. In contrast, Fig. 4d demonstrates an increase in small strain area size, with the small strain values remaining relatively stable, achieved by modulating the groove depths. To substantiate the observed alterations in small strain value, we calculated the mean strain values across the small strain areas, demarcated by the red rectangular frame in Fig. 4e. The mean small strain values of the first set of PGSSs decrease as groove depth increases, while those of the second set remain constant (Fig. 4f, g). In addition, the mean values of the large strain areas were also quantitatively calculated, as shown in Fig. S8. The reduction in small strain value, combined with the increase in small strain proportion, progressively amplifies localized large strain value.

The strain analysis conducted thus far suggests that the structural design of the PGSSs aligns well with our proposed design guideline for heterogeneous strain engineering. With appropriate parameter setup and the application of a constant electric current in the FEA models, the strain sensing responses of the PGSSs were predetermined, as presented in Fig. 4h, i. In the first set of PGSSs, where a constant small strain proportion is maintained, the 80–400 sensor exhibits the lowest small strain value and the highest sensitivity, outperforming the 60–400 sensor, which in turn surpasses the 40–400 sensor. In the second set of PGSSs, the 80–300 sensor exhibits the highest small strain proportion and the highest sensitivity, followed by the 70–250 sensor and then by the 60–200 sensor. In Fig. 4h, i, the subplots on the right display the electric potential distribution of each sensor when subjected to 100% applied strain. It is evident that under the same uniaxial tensile strain, a greater potential drop corresponds to a larger change in resistance. It is worth noting that when the applied strain is below 50%, the resistance change is approximately the same across the different PGSSs. This behavior arises due to the relatively small difference between small strain value and large strain value. The surface strain distributions of the PGSSs at 50% applied strain are depicted in Fig. S9. It is evident that for all structural patterns, the discrepancy between large strain value and small strain value is substantially smaller than that observed at 100% applied strain. Given the exponential relationship between relative resistance change and strain, the superiority of the resistance gain in large strain areas is inherently limited when compared to the losses in small strain areas. The strain sensing responses of the PGSSs, as determined by FEA, align perfectly with the trends outlined by the Monte Carlo simulations, thereby confirming the reliability and feasibility of the quantitative design guideline.

Fabrication and structural features of PGSSs

To further substantiate the feasibility of the optimal heterogeneous strain topology, we fabricated physical PGSSs in accordance with the FEA models (Fig. S10). Firstly, as shown in Fig. 5a, two sets of hollow stainless-steel templates (Fig. S11) with different thicknesses and inter-opening spacings, but identical opening widths, were customized based on the groove parameters from the FEA models. After employing stainless-steel templates and convex PDMS (Figs. S12 and S13) as primary and secondary molds, respectively, two sets of concave PDMS substrates featuring different groove depths and inter-groove spacings were obtained. The cross-sectional views of the PDMS substrates are presented in Fig. 5b, c, and the top-down views in Figs. S14 and S15. It can be observed that for the first set of PDMS

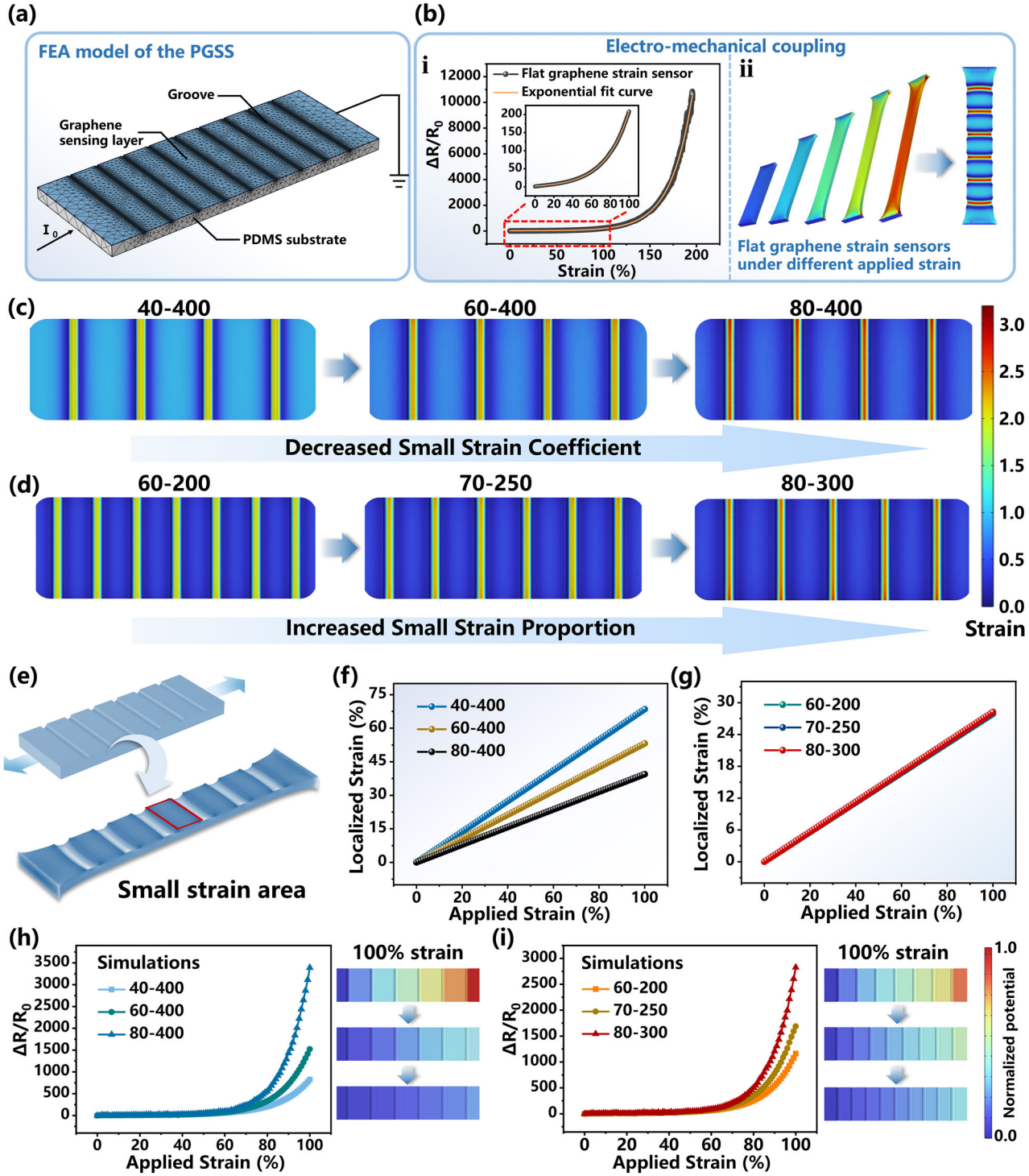

Fig. 4 | FEA simulations of PGSSs. a The FEA formulation of PGSSs. **b** Electro-mechanical coupling: (i) the sensing response of an unpatterned graphene strain sensor, (ii) the surface strain distribution of a PGSS. **c**, **d** The optimal heterogeneous strain distributions of PGSSs at 100% applied strain: (**c**) increased groove depths (40 → 60 → 80 μm) at constant 400 μm inter-groove spacing, (**d**) increased groove depths (60 → 70 → 80 μm) and inter-groove spacings (200 → 250 → 300 μm). **e** Definition of small strain area. **f**, **g** The mean small strain values of PGSSs at different applied strains. **h**, **i** The sensing responses of PGSSs and the electric potential distributions.

substrates, the groove depths are 40, 60, and 80 μm, with a consistent inter-groove spacing of 400 μm. For the second set of PDMS substrates, the groove depths are 60, 70, and 80 μm, with corresponding inter-groove spacings of 200, 250, and 300 μm. The groove depth and inter-groove spacing of each PDMS substrate perfectly replicate the microstructure of the corresponding stainless-strain template, thanks to the extremely low surface tension of liquid PDMS. After oxygen plasma treatment and a spray-coating process, the PGSSs were physically obtained (Fig. S16). Figure 5d demonstrates the progressive hydrophilization of PDMS surfaces under prolonging oxygen plasma treatment, with contact angles decreasing from 110.35° to 10.56°. Comparative XPS analysis (Fig. S17, Table S1) reveals a significant increase in surface oxygen content from 29.55% to 45.23%. The high-resolution O 1 s spectrum, presented in Fig. 5e, shows two distinct peaks at 532.7 eV and 533.4 eV, corresponding to Si-O-Si and -OH species, respectively[28]. The

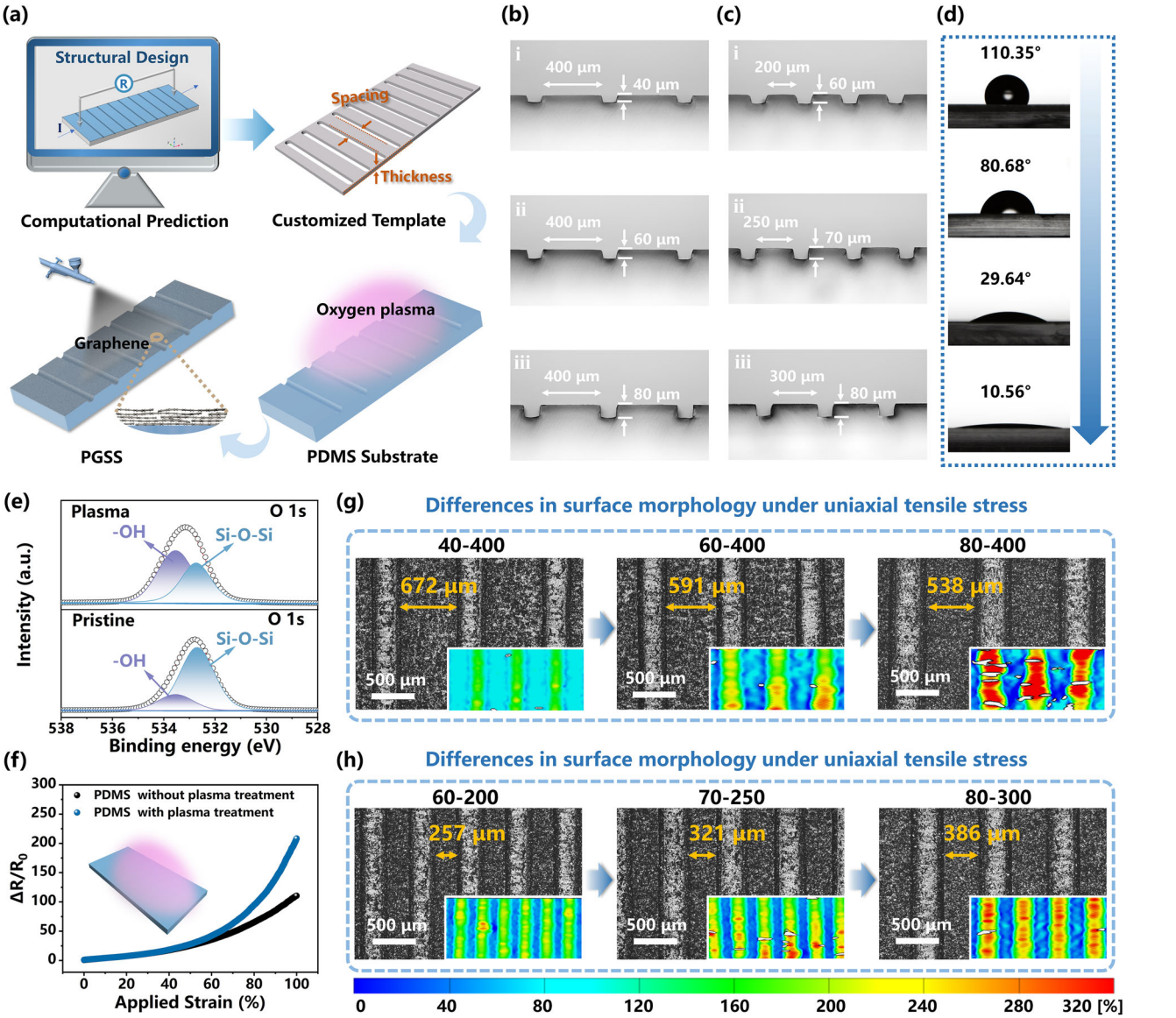

Fig. 5 | Fabrication and structural features of PGSSs. a The fabrication process of PGSSs. **b**, **c** The cross-sectional views of resultant concave PDMS substrates. **d** The contact angles of PDMS surfaces after 0−4 minutes of oxygen plasma treatment. **e** O 1 s spectra of PDMS surfaces. **f** The strain sensing responses of unpatterned graphene sensors. **g**, **h** The top-down views and strain distributions (insets) of PGSSs at 100% applied strain.

oxygen plasma-treated surface, which possesses a higher concentration of -OH groups than the pristine surface, demonstrates a marked enhancement in surface hydrophilicity. The enhanced surface hydrophilicity promotes uniform solvent spreading during spray-coating, enabling the formation of homogeneous, dense graphene films upon solvent evaporation (Fig. S18). Surface roughness measurements further confirm more uniform graphene coverage on plasma-treated PDMS (Fig. S19). Such optimized morphology facilitates effective strain transfer from the PDMS substrate to the top graphene layer. With the same initial resistance, an unpatterned graphene strain sensor with an oxygen plasma-treated PDMS substrate output a significantly enhanced resistance change compared to that of a sensor with a pristine PDMS substrate, as shown in Fig. 5f.

The morphologies of the six PGSSs at 100% applied strain are presented in Fig. 5g, h, all captured at the same magnification. The detailed morphological changes during the stretching processes are shown in Figs. S20 and S21. It is clearly observable that the graphene nanoflakes within the grooved regions exhibit sparser coverage than those in the inter-groove regions. This is attributed to the greater lateral movement of graphene, driven by the intensified deformations of the grooved regions of the patterned PDMS substrates upon stretching. The diminished overlap and interconnection between the graphene nanoflakes within the grooved regions lead to a marked elevation in resistance, which is a crucial aspect to the enhanced sensitivity. In the first set of PGSSs, a discernible progressive narrowing of the inter-groove regions is observed in Fig. 5g, indicating a reduction in small strain value. Upon measurement and calculation, the actual small strain values of the PGSSs are found to be 68.0%, 47.8%, and 34.5%, consistent with the trend predicted by the FEA simulations. For the second set of PGSSs, the initial inter-groove spacings measure 200, 250, and 300 μm. When subjected to 100% applied strain, the increases in inter-groove spacing are ~57, 71, and 86 μm, as shown in Fig. 5h. Therefore, the actual small strain values are 28.5%, 28.4%, and 28.7%, consistent with the structural design requirement of maintaining a fixed small strain value while gradually increasing small strain proportion. The insets illustrate the surface strain distributions of the PGSSs, characterized by the digital image correlation (DIC) technique. The detailed variations in surface strain distribution during the stretching processes are illustrated in Figs. S22 and S23, as well as in Supplementary Movies 1–6. The DIC characterization results also clearly indicate that in both systems, large strain value gradually increases, which is

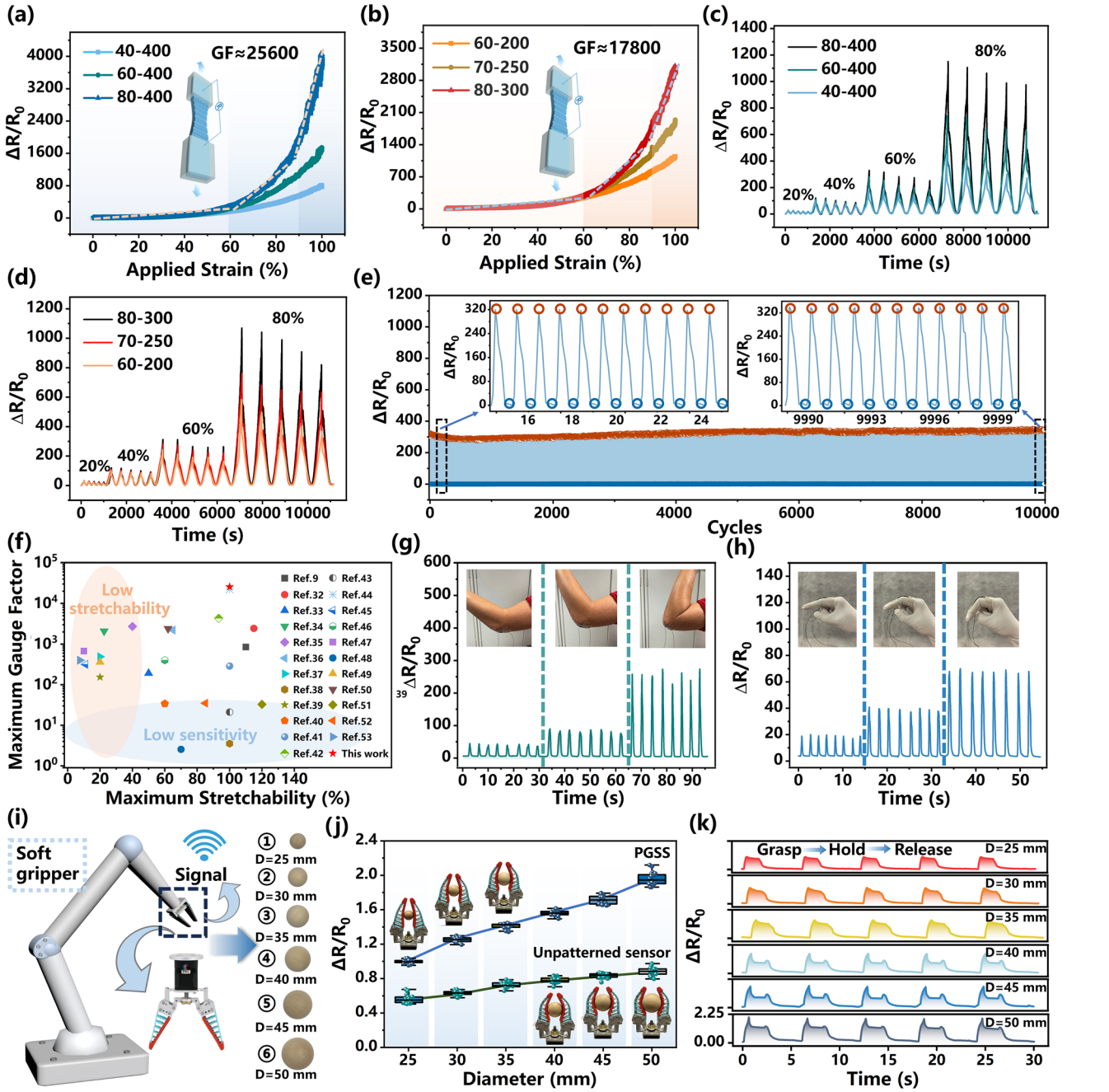

Fig. 6 | Experimental analysis of PGSSs. a—**d** The strain sensing responses of PGSSs (in (**a**, **b**), the dotted lines signify the segments over which gauge factors are calculated; the gauge factors presented indicate the values at 100% applied strain). **e** Stability evaluation of the 80–400 sensor under 10,000 stretching cycles at 60% applied strain. **f** Comparative analysis of strain sensing performance: the 80–400 sensor vs. state-of-the-art graphene-based sensors. Monitoring of the cyclic bending of the (**g**) elbow and (**h**) finger to varying degrees. **i** Integration of the 80–400 sensor with a robot gripper for object size feedback. **j** The resistance changes of the 80–400 sensor and an unpatterned sensor during the grasping of balls of different sizes. **k** The resistance changes of the 80–400 sensor when handling balls of different sizes.

achieved by either increasing small strain proportion or decreasing small strain value. A comparative analysis of the DIC results and FEA results demonstrates that the trends in heterogeneous strain distribution, as predicted numerically and obtained experimentally, are completely consistent. The discrepancy in actual strain value between the two sets of results is likely due to the inherent resolution constraints of the DIC technique.

Sensing performance analysis of PGSSs

The trends in relative resistance change, calculated via the FEA simulations, have been experimentally replicated, as shown in Fig. 6a, b. The relative resistance change vs. strain curves can be categorized into three regions, each corresponding to a distinct gauge factor (Table S2). The gauge factor of each region is calculated as the slope of the corresponding section of the curve, defined by $GF = (\Delta R/R_0)/\Delta\varepsilon$[7,29–31]. Among the first set of PGSSs, the 80–400 sensor demonstrates the highest gauge factor across all applied strain levels, while in the second set, the 80–300 sensor is the one that shows the superior overall performance. Furthermore, at 100% applied strain, the gauge factors for the 80–400 sensor, 60–400 sensor, and 40–400 sensor were calculated to be 25600, 11500, and 2400. Similarly, the gauge factors for the 80–300 sensor, 70–250 sensor, and 60–200 sensor were 17,800, 11,900, and

5,400. The decrease in small strain value and increase in small strain proportion significantly enhance sensitivity, yielding a ~10.7-fold and ~3.3-fold improvement at 100% applied strain, respectively. The gauge factors of the PGSSs substantially exceed that of the unpatterned graphene strain sensor, which exhibits a gauge factor of only 840. Although there exist certain differences between the specific values of the numerically predicted relative resistance changes and those of experimental obtained results, the overall trends are consistent: the 80–400 and 80–300 sensors exhibit the highest sensitivity in their respective group, while the 40–400 and 60−200 sensors demonstrate the lowest. Such discrepancies may be attributed to subtle structural differences between the FEA models and the experimental specimens, as well as to potential disparities between the actual resistance values at high strain levels (>200%) and the resistance values obtained by extrapolating the resistance-strain relationship which was experimentally measured over a smaller strain range. The strain sensing responses of all PGSSs are almost repeatable under cyclic strains ranging from 20% to 80% (Fig. 6c, d). The slight degradation in resistance change may be attributed to the imperfect adhesion between graphene and PDMS substrate. Cross-sectional characterization of the PGSSs before and after strain application revealed no observable interfacial delamination between PDMS substrate and graphene sensing layers, confirming the mechanical stability of the sensor structure (Fig. S24). To evaluate the detection capability of the PGSSs for subtle strains, the resistance fluctuations under zero-strain condition were acquired (Fig. S25). Statistical analysis of the time-dependent resistance changes revealed the exceptional stability of the sensors with the standard deviations (σ) sitting at merely 0.024-0.062%. Further, the strain sensing responses of the PGSSs were characterized through controlled testing within 1% applied strain. The results demonstrated high signal fidelity with minimal noise interference (Fig. S26). All sensor configurations showed steady and well-defined relative resistance change-strain relationships within this low strain regime. These findings collectively validate the reliable performance of the PGSSs for applications requiring precise detection of minute mechanical deformations.

Figure 6e demonstrates the operational stability of the 80–400 sensor through 10,000 consecutive load/unload cycles at 60% applied strain. The strain sensing response curve demonstrates consistent peak values with negligible drift during prolonged cyclic operation at high applied strain level, confirming exceptional electromechanical stability. It is noteworthy that the overall performance of the 80–400 sensor, encompassing both sensitivity and stretchability, exceeds those of other recently reported graphene-based strain sensors[9,32–53], as depicted in Fig. 6f. Furthermore, when compared with heterogeneous strain sensors employing different novel structural configurations or active sensing materials (Table S3), our sensor still demonstrates superior sensitivity and sensing range. Upon integrating the 80–400 sensor, which exhibits the highest sensitivity, onto a finger and an elbow joint, we observed a progressive increase in resistance change that directly correlates with the degree of bending (Fig. 6g, h), thereby substantiating the efficacy of the PGSS in monitoring human body motions. Figure 6i illustrates the surface-mounting of the 80–400 sensor and an unpatterned sensor on a compliant two-finger robot gripper, where volumetric estimation of grasped objects is made possible by real-time strain monitoring. Indeed, the bending deformation of the soft gripper during object grasping induces localized strain amplification in the PGSS, thereby enabling higher sensitivity and accuracy in dimension assessment. In Fig. 6j, it is demonstrated that the 80–400 sensor exhibits superior sensitivity compared to its unpatterned graphene counterpart, showing more pronounced differences between the signals for spherical objects of varying sizes. The resistance responses of the 80–400 sensor were further evaluated through complete gripping cycles (grasp-hold-release), as presented in Fig. 6k. From the size-dependent signal profiles, excellent repeatability is observed across the multiple gripping cycles for each object, confirming the reliability of the PGSS.

Diverse implementation of the optimal heterogeneous strain structure

The incorporation of heterogeneous strain distribution represents an emerging strategy with immense potential to enhance the sensitivity of strain sensors. This strategy effectively circumvents complex interfacial interactions within the conductive layers of composite sensors and enables flexible adjustment of sensor sensitivity. Its universal applicability allows for deployment across a wide range of structures and materials. Two primary approaches are employed to create heterogeneous strain distributions in strain sensors: customizing structural patterns on a sensor and manipulating the intrinsic material properties, both of which are aimed at inducing stress concentration. While the PGSS exemplifies the customization of structural patterns, another graphene-based sensor demonstrates an approach to manipulating material properties, as detailed in Supplementary Note S2 and Figs. S27–S29. Specifically, a heterogeneous strain distribution is achieved on a sensor by partitioning the substrate into two distinct regions, characterized by differing elastic modulus: one region possessing a high elastic modulus, and the other exhibiting a low elastic modulus. The two control parameters, i.e., small strain value and small strain proportion, are modulated by adjusting the magnitudes of the high and low elastic modulus, as well as by modifying the ratio between the sizes of the two types of regions. We established FEA models to study the structural features and strain sensing responses of the sensor. The results verify the applicability of the quantitative design guideline for heterogeneous strain engineering in guiding material property manipulation to enhance sensitivity. In summary, the optimal heterogeneous strain topology, characterized by its versatility in sensitivity tuning and its adaptability to a variety of sensing structures and materials, holds considerable potential for deployment in the field of wearable electronics.

Discussion

In summary, we proposed a heterogeneous strain framework that establishes the relationship between the local resistance changes at the microscale and the macroscopic sensing performance and derived the optimal heterogeneous topology and quantitative design guideline for computational design of ultra-sensitive strain sensors. Specifically, Monte Carlo simulations reveal that the sensitivity enhancement achieved under the optimal heterogeneous strain structure is predominantly determined by the strain amplification in large strain areas and modulated by the properties of small strain regions. Corresponding mathematical proof elucidates the contributions of decreased small strain value and increased small strain proportion. A PGSS was conceptualized as a computational design case to validate the feasibility of the quantitative design guideline. The concordance between the sensing trajectories of physical PGSSs and the corresponding computational predictions not only corroborates the fidelity of the FEA models but also adheres to the trend projected by the Monte Carlo simulations. At 100% applied strain, reducing small strain value and increasing small strain proportion can significantly enhance the sensitivity of the PGSS by factors of approximately 10.7 and 3.3, respectively. The highest gauge factors achieved by the two means of modulation were 25,600 and 17,800, respectively, whereas the gauge factor of the benchmark unpatterned graphene sensor was only 840. This design principle has also been successfully extended to other sensor systems, thereby endowing it with substantial practical significance in the development of high-performance flexible electronics.

Methods

Monte Carlo simulations

At the initial stage, a 2D (5 × 6) matrix of nodes was defined, where a resistor was inserted between each adjacent pair of nodes along each row, resulting in a 5 × 5 resistor network as depicted in Fig. S1. For each random heterogeneous strain distribution, characterized by a distinct combination of small strain proportion, small strain coefficient, and positions of small strain units, the small strain value and large strain value were calculated according to $N_s C\varepsilon_a + (1 - N_s)\varepsilon_l = \varepsilon_a$ and $\varepsilon_s = C\varepsilon_a$, and the resistance for each strain unit was computed based on the resistance-strain relationship of an unpatterned graphene strain sensor (Fig. S2). Boundary conditions were rigorously applied within the resistor network, with one boundary designated as the ground and the opposite boundary subjected to a constant

electric potential. Based on the calculated resistances between connected nodes, the electric potential distribution across the entire resistor network was determined. Finally, the input electric current was evaluated, enabling the computation of the total resistance of the network. This approach allows for a comprehensive assessment of the resistance behavior of the network under varying heterogeneous strain distributions.

FEA simulations

The multiphysics-based 3D FEA models of PGSSs were constructed, as shown in Fig. S30. The upper surface of each sample is set as a graphene conductive layer whose conductivity changes with strain, while the bottom section is set as a PDMS substrate. The material properties of PDMS include Young's modulus 750 kPa, density 0.97 g/cm3, and Poisson's ratio 0.49. The correlation between conductivity and strain is derived from the resistance-strain relationship of an unpatterned graphene strain sensor. In each FEA simulation, the left edge of the model is fixed, the right edge is pulled along the x-direction, and translation along the y- and z-direction is restrained. The total resistance of the system can be calculated by setting the input current as a constant value and calculating the potential distribution of the conductive layer according to the surface strain distribution of the conductive layer. All FEA simulations were performed using COMSOL Multiphysics® 6.0 with the default segregated solvers (PARDISO for structural mechanics and MUMPS for electrical analysis) and a relative tolerance of 0.1% as the convergence criterion.

Fabrication of unpatterned graphene strain sensors

Liquid PDMS and crosslinker (SYLGARD 184, Dow Corning, USA) were mixed at a ratio of 10:1 and stirred for 30 minutes, followed by a degassing process in a vacuum oven for 20 minutes. The degassed PDMS was poured into a square petri dish and cured at room temperature for three days. The cured flat PDMS substrate was then peeled from the dish and cut into 80 mm × 10 mm strips. Elastic conductive adhesive was coated onto both ends of each strip to form electrodes, with careful control to ensure that the distance between the electrodes remained consistent across all the strips. After complete curing, the PDMS substrates were treated with oxygen plasma. Graphene nanosheets (diameter: 5–10 μm, thickness: 3−10 nm; Nanjing XFNANO Materials Tech, China) were dispersed in isopropyl alcohol solvent (Anaqua Chemicals Supply, USA) and ultrasonicated for six hours. The graphene dispersion was then spray-coated onto the surface of the PDMS substrates. During the spray-coating process, the amount of graphene was carefully controlled to ensure that the initial resistances of the resultant sensors remained consistent at approximately 10 kΩ. To measure the resistances of the sensors, copper wires were affixed to the electrodes using silver paste. For comparison, an unpatterned graphene strain sensor without plasma treatment was fabricated following the same procedure. The fabrication process is illustrated in Fig. S31.

Fabrication of PGSSs

A customized stainless-steel template was attached to the inner bottom surface of a square petri dish. Degassed liquid PDMS, prepared in the same way as in "Fabrication of unpatterned graphene strain sensors", was poured into the petri dish and cured at room temperature for three days. The resultant PDMS sheet with a convex pattern was peeled from the stainless-steel template, heat-treated in a tube furnace at 400 °C for three minutes, and then attached to the inner bottom surface of a new square petri dish with its convex pattern facing upward. The same degassed liquid PDMS was poured into the petri dish and allowed to cure completely. The resultant PDMS sheet with a concave pattern was peeled from the convex PDMS template and cut into 80 mm × 10 mm strips. The remaining fabrication steps, which include the installation of electrodes and wires, the oxygen plasma treatment of PDMS, and the preparation and spray-coating of graphene dispersion, followed the same procedures as outlined in "Fabrication of unpatterned graphene strain sensors".

Characterization

Oxygen plasma treatment of PDMS was carried out using a plasma cleaner (Harrick Plasma, USA). An X-ray photoelectron spectrometer (Nexsa G2, Thermo Fisher Scientific, USA) was used to quantify the surface chemical compositions of PDMS before and after oxygen plasma treatment. The wettability of PDMS was measured using a contact angle meter. A white-light interferometer (TopMap Metro.Lab, Polytec, Germany) was used to characterize the surface roughness of graphene-coated PDMS. The top morphologies of the PGSS samples were observed using a field emission scanning electron microscope (JSM7100, JOEL, Japan). The cross-sectional morphologies, as well as the changes in top morphology during stretching, were observed under an optical microscope (BX43, Olympus, Japan). The resistances of the PGSS samples were measured by a digital multimeter (DMM6500, Keithley Instruments, USA). The tensile tests were carried out on a desktop universal testing machine (ZQ-990L, Dongguan Zhiqu Precision Instruments, China).

Data availability

The datasets generated during and/or analyzed during the current study are available from the corresponding author on reasonable request.

Code availability

The computer codes supporting the current study are available from the corresponding author upon reasonable request.

Received: 3 April 2025; Accepted: 5 September 2025;
Published online: 22 October 2025

References

1. Pan, D. et al. Biomimetic wearable sensors: emerging combination of intelligence and electronics. *Adv. Sci.* **11**, 2303264 (2024).
2. Huang, X. et al. High-stretchability and low-hysteresis strain sensors using origami-inspired 3D mesostructures. *Sci. Adv.* **9**, 9799 (2023).
3. Wang, M. et al. Gesture recognition using a bioinspired learning architecture that integrates visual data with somatosensory data from stretchable sensors. *Nat. Electron.* **3**, 563–570 (2020).
4. Duan, L., D'hooge, D. R. & Cardon, L. Recent progress on flexible and stretchable piezoresistive strain sensors: from design to application. *Prog. Mater. Sci.* **114**, 100617 (2020).
5. Gao, Z. et al. Advances in wearable strain sensors based on electrospun fibers. *Adv. Funct. Mater.* **33**, 2214265 (2023).
6. Liu, Y. et al. Ag–thiolate interactions to enable an ultrasensitive and stretchable MXene strain sensor with high temporospatial resolution. *Nat. Commun.* **15**, 5354 (2024).
7. Araromi, O. A. et al. Ultra-sensitive and resilient compliant strain gauges for soft machines. *Nature* **587**, 219–224 (2020).
8. Mei, S. et al. High-density, highly sensitive sensor array of spiky carbon nanospheres for strain field mapping. *Nat. Commun.* **15**, 3752 (2024).
9. Yoon, H. et al. In Situ Co-transformation of reduced graphene oxide embedded in laser-induced graphene and full-range on-body strain sensor. *Adv. Funct. Mater.* **33**, 2300322 (2023).
10. Wang, X., Qu, M., Wu, K., Schubert, D. W. & Liu, X. High sensitive electrospun thermoplastic polyurethane/carbon nanotubes strain sensor fitting by a novel optimization empirical model. *Adv. Compos. Hybrid. Mater.* **6**, 63 (2023).
11. Cuthbert, T. J., Hannigan, B. C., Roberjot, P., Shokurov, A. V. & Menon, C. HACS: Helical auxetic yarn capacitive strain sensors with sensitivity beyond the theoretical limit. *Adv. Mater.* **35**, 2209321 (2023).
12. Jiang, Y. et al. Auxetic mechanical metamaterials to enhance sensitivity of stretchable strain sensors. *Adv. Mater.* **30**, 1706589 (2018).
13. Li, S. et al. Bioinspired robot skin with mechanically gated electron channels for sliding tactile perception. *Sci. Adv.* **8**, 0720 (2022).

14. Shi, X. et al. Bioinspired ultrasensitive and stretchable MXene-based strain sensor via nacre-mimetic microscale "brick-and-mortar" architecture. *ACS Nano* **13**, 649–659 (2019).
15. Zhou, R. et al. Hierarchical synergistic structure for high resolution strain sensor with wide working range. *Small* **19**, e2301544 (2023).
16. Jin, Q., Liu, Z., Ouyang, X., Liu, Y. & Wang, X. Superhydrophobic MXene-CNT bridge strain sensors with wide linear-range via strain-isolation and crack-synergy effects. *Chem. Eng. J.* **488**, 150796 (2024).
17. Jiang, Y., Liu, Z., Wang, C. & Chen, X. Heterogeneous strain distribution of elastomer substrates to enhance the sensitivity of stretchable strain sensors. *Acc. Chem. Res.* **52**, 82–90 (2019).
18. Shao, H. et al. Elastic Janus microarray film strain sensors with heterogeneous modulus and conductivity for healthcare and braille identification. *Adv. Funct. Mater*. **34**, 2316134 (2024).
19. Luo, Y. et al. Heterogeneous strain distribution based programmable gated microchannel for ultrasensitive and stable strain sensing. *Adv. Mater.* **35**, 2207141 (2023).
20. Kim, Y.-G., Song, J.-H., Hong, S. & Ahn, S.-H. Piezoelectric strain sensor with high sensitivity and high stretchability based on kirigami design cutting. *npj Flex. Electron.* **6**, 52 (2022).
21. Luo, Y. et al. Flexible liquid metal-based microfluidic strain sensors with fractal-designed microchannels for monitoring human motion and physiological signals. *Biosens. Bioelectron.* **246**, 115905 (2024).
22. Hu, T. & Sheng, B. A highly sensitive strain sensor with wide linear sensing range prepared on a hybrid-structured CNT/Ecoflex film via local regulation of strain distribution. *ACS Appl. Mater. Interfaces* **16**, 21061−21072 (2024).
23. Zhuo, F. et al. Kirigami-inspired 3D-printable MXene organohydrogels for soft electronics. *Adv. Funct. Mater*. **33**, 2308487 (2023).
24. Jia, J. et al. Janus and heteromodulus elastomeric fiber mats feature regulable stress redistribution for boosted strain sensing performance. *ACS Nano* **16**, 16806–16815 (2022).
25. Pan, S. et al. Mechanocombinatorially screening sensitivity of stretchable strain sensors. *Adv. Mater.* **31**, 1903130 (2019).
26. Weng, Z., Zou, F., Li, D. & Yao, Y. A high-sensitivity thin-film MWNT@PDA-AgNP nanocomposite sensor for acquiring microscopic deformations. *Compos. Sci. Technol.* **229**, 109689 (2022).
27. Wu, Y. et al. A review of flexible strain sensors based on natural fiber materials. *Adv. Mater. Technol.* **8**, 2201503 (2023).
28. Jiang, B., Guo, H., Chen, D. & Zhou, M. Microscale investigation on the wettability and bonding mechanism of oxygen plasma-treated PDMS microfluidic chip. *Appl. Surf. Sci.* **574**, 151704 (2022).
29. Fu, Y. et al. Ultraflexible temperature-strain dual-sensor based on chalcogenide glass-polymer film for human-machine interaction. *Adv. Mater*. **36**, e2313101 (2024).
30. Kim, T. et al. Ultra-stable and tough bioinspired crack-based tactile sensor for small legged robots. *npj Flex. Electron.* **7**, 22 (2023).
31. Yang, Y. et al. A high-sensitive rubber-based sensor with integrated strain and humidity responses enabled by bionic gradient structure. *Adv. Funct. Mater.* **34**, 2400789 (2024).
32. Zhu, W. et al. Flexible strain sensor based on copper/graphene composite films. *ACS Appl. Nano Mater.* **7**, 358–369 (2024).
33. Wang, W. et al. Fingerprint-inspired strain sensor with balanced sensitivity and strain range using laser-induced graphene. *ACS Appl. Mater. Interfaces* **14**, 1315–1325 (2022).
34. Zhang, S. et al. On-skin ultrathin and stretchable multifunctional sensor for smart healthcare wearables. *npj Flex. Electron.* **6**, 11 (2022).
35. Chen, X. et al. A laser-scribed wearable strain sensing system powered by an integrated rechargeable thin-film zinc-air battery for a long-time continuous healthcare monitoring. *Nano Energy* **101**, 107606 (2022).
36. Chen, X. et al. Porous graphene foam composite-based dual-mode sensors for underwater temperature and subtle motion detection. *Chem. Eng. J.* **444**, 136631 (2022).
37. Liu, W. et al. In situ laser synthesis of Pt nanoparticles embedded in graphene films for wearable strain sensors with ultra-high sensitivity and stability. *Carbon* **190**, 245–254 (2022).
38. Raza, T. et al. Wearable and flexible multifunctional sensor based on laser-induced graphene for the sports monitoring system. *ACS Appl. Mater. Interfaces* **14**, 54170–54181 (2022).
39. Cheng, X., Cai, J., Xu, J. & Gong, D. High-performance strain sensors based on Au/graphene composite films with hierarchical cracks for wide linear-range motion monitoring. *ACS Appl. Mater. Interfaces* **14**, 39230–39239 (2022).
40. Wang, G., Wang, M., Zheng, M., Yao, S. & Ebo, B. High-sensitivity GNPs/PDMS flexible strain sensor with a microdome array. *ACS Appl. Electron. Mater.* **4**, 4576–4587 (2022).
41. Zhang, H. et al. Anisotropic, wrinkled, and crack-bridging structure for ultrasensitive, highly selective multidirectional strain sensors. *Nano Micro Lett.* **13**, 122 (2021).
42. Luo, Z. et al. In situ dynamic manipulation of graphene strain sensor with drastically sensing performance enhancement. *Adv. Electron. Mater.* **6**, 2000269 (2020).
43. Li, B. et al. A highly stretchable, super-hydrophobic strain sensor based on polydopamine and graphene reinforced nanofiber composite for human motion monitoring. *Compos. Part B Eng.* **181**, 107580 (2020).
44. Deng, C. et al. Ultrasensitive and highly stretchable multifunctional strain sensors with timbre-recognition ability based on vertical graphene. *Adv. Funct. Mater.* **29**, 1907151 (2019).
45. Chen, X. et al. A dual-functional graphene-based self-alarm health-monitoring e-skin. *Adv. Funct. Mater.* **29**, 1904706 (2019).
46. Zhang, R. et al. A bubble-derived strategy to prepare multiple graphene-based porous materials. *Adv. Funct. Mater.* **28**, 1705879 (2018).
47. Qiao, Y. et al. Multilayer graphene epidermal electronic skin. *ACS Nano* **12**, 8839–8846 (2018).
48. Han, J., Lee, J., Lee, J. & Yeo, J. Highly stretchable and reliable, transparent and conductive entangled graphene mesh networks. *Adv. Mater.* **30**, 1704626 (2018).
49. Chen, Z., Liu, X., Wang, S., Zhang, X. & Luo, H. A bioinspired multilayer assembled microcrack architecture nanocomposite for highly sensitive strain sensing. *Compos. Sci. Technol.* **164**, 51–58 (2018).
50. Shi, X., Liu, S., Sun, Y., Liang, J. & Chen, Y. Lowering internal friction of 0D-1D-2D ternary nanocomposite-based strain sensor by fullerene to boost the sensing performance. *Adv. Funct. Mater.* **28**, 1800850 (2018).
51. Wu, S., Peng, S., Han, Z. J., Zhu, H. & Wang, C. H. Ultrasensitive and stretchable strain sensors based on mazelike vertical graphene network. *ACS Appl. Mater. Interfaces* **10**, 36312–36322 (2018).
52. Cai, Y. et al. Extraordinarily stretchable all-carbon collaborative nanoarchitectures for epidermal sensors. *Adv. Mater.* **29**, 1606411 (2017).
53. Wang, D.-Y. et al. High performance flexible strain sensor based on self-locked overlapping graphene sheets. *Nanoscale* **8**, 20090–20095 (2016).

Acknowledgements

This work is supported by the Research Center for Nature-Inspired Science and Technology, The Hong Kong Polytechnic University (Project No.: CE1T).

Author contributions

Conceptualization: W.W., F.Z.; Methodology: W.W., T.W., M.G., F.Z., F.C., Z.W.; Software: W.W., T.W.; Validation: W.W.; Formal analysis: W.W., T.W., M.G., F.Z., F.C., Z.W.; Investigation: W.W., T.W., M.G., F.Z., F.C., Z.W.; Resources: F.Z.; Data Curation: W.W., M.G., F.C.; Writing—Original Draft: W.W.; Writing—Review and Editing: F.Z.; Visualization: W.W.; Supervision: F.Z.; Project administration: F.Z.; Funding acquisition: F.Z.

Competing interests
The authors declare no competing interests.

Additional information
Supplementary information The online version contains supplementary material available at https://doi.org/10.1038/s41528-025-00483-8.

Correspondence and requests for materials should be addressed to Fangxin Zou.